ENGINEERING

A fully integrated breathable haptic textile

Kuanming Yao[1]†, Qiuna Zhuang[2]†, Qiang Zhang[1]†, Jingkun Zhou[1,3]†, Chun Ki Yiu[1,3], Jianpeng Zhang[1], Denglin Ye[1], Yawen Yang[1], Ki Wan Wong[1], Lung Chow[1], Tao Huang[4], Yuze Qiu[1,5], Shengxin Jia[1,3], Zhiyuan Li[1], Guangyao Zhao[1], Hehua Zhang[1], Jingyi Zhu[1], Xingcan Huang[1], Jian Li[1,3], Yuyu Gao[1], Huiming Wang[2], Jiyu Li[1,3], Ya Huang[1], Dengfeng Li[1], Binbin Zhang[1,3], Jiachen Wang[1], Zhenlin Chen[1], Guihuan Guo[1], Zijian Zheng[2,6,7,8,9]*, Xinge Yu[1,3,10]*

Wearable haptics serve as an enhanced media to connect humans and VR/robots. The inevitable sweating issue in all wearables creates a bottleneck for wearable haptics, as the sweat/moisture accumulated in the skin/device interface can substantially affect feedback accuracy, comfortability, and create hygienic problems. Nowadays, wearable haptics typically gain performance at the cost of sacrificing the breathability, comfort, and biocompatibility. Here, we developed a fully integrated breathable haptic textile (FIBHT) to solve these trade-off issues, where the FIBHT exhibits high-level integration of 128 pixels over the palm, great stretchability of 400%, and superior permeability of over 657 g/m^2/day (moisture) and 40 mm/s (air). It is a stand-alone haptic system totally composed of stretchable, breathable, and bioadhesive materials, which empowers it with precise, sweating/movement-insensitive and dynamic feedback, and makes FIBHT powerful for virtual touching in broad scenarios.

INTRODUCTION

Attaining fine haptic perception from our largest sensing organ, skin, could enable people to acquire more information (*1*). To fulfill the requirements of haptics in daily life, various technologies have been adapted into consumer electronics, including vibration joystick gamepads, microvibration motors in phones, etc. In recent years, wearable haptic interfaces have attracted a lot of attention, as they can release our hands to experience virtual touching without grasping external instruments (*2, 3*). The indispensable role of wearable haptics includes the following: the virtual objects need to be vividly felt by users in virtual/augmented reality (VR/AR), a patient with peripheral neural disease or deterioration wishes to recover natural touching perceptions on a patient's hands, an amputee trying to regain tactile sense from the neuroprosthetic, etc.

Flexible/soft electronic technologies (*4–11*) have been proven to be the foundation for wearable human-machine interfaces (*12, 13*) and especially haptic interfaces. Examples include pneumatic haptic gloves (*14*), wearable vibrohaptic systems (*15–21*), electrotactile patches (*22–29*), origami-based active haptics (*30*), thermal gloves (*31–33*), multimodal systems (*34*), etc. However, challenges remain. Balancing the large feedback coverage area (e.g., the whole hand) and high spatial resolution is critical, as high-density feedback units' array will substantially complicate the design and integration. Furthermore, similar to other wearable devices (e.g., heavy VR headsets), the deficit in wearing comfort is a common user complaint. In haptic interfaces, skin-interfaced electronic designs allowing the skin to breathe are urgently needed, which on one hand can minimize the device weight and on the other hand can solve unstable operation properties that may occur due to skin occlusion, especially when sweating (*35, 36*). This point is especially critical for hands, since our hands produce the most sweat (*37, 38*) (text S1). However, the current electronic systems for such haptic interfaces are typically unstretchable, impermeable, and with low unit density and low adhesion to skin, which have a great distance to meet the requirement of high-level VR/AR applications.

Here, we report a class of materials, devices, and system-level integration strategies for developing a fully integrated breathable haptic textile (FIBHT). The FIBHT features a large-area, high-resolution electrotactile electrode array that empowers precise dynamic feedback on the hand. The system uses electrospun poly(styrene-*block*-butadiene-*block*-styrene) (SBS) fiber as a substrate, ensuring excellent permeability to air and moisture (*39*). This allows sweat to evaporate, keeping skin dry and comfortable during use and prevents skin from itchiness or inflammation. With an innovative assembly strategy (*40–42*), we built the complete system and skin interfaces in one single piece comprising a permeable SBS fiber mat, liquid metal (LM), (*43–46*) and bioadhesive hydrogels (*47–49*). Hence, the FIBHT is ultrasoft, stretchable, and adheres firmly to the skin, adapting to natural hand motions. The high electrode density of ~1 pixel/cm² (overall) and 2.26 pixel/cm² in the fingertips region (fig. S1) allows the FIBHT to exhibit great spatiotemporal resolution for dynamic feedback with ultrastable properties under both dry and wet conditions. In terms of permeability, stretchability, adhesiveness, and system-level integrality, the FIBHT outperforms existing haptic wearables (table S1), making haptics more comfortable and closer to real experiences.

## RESULTS

Design of the FIBHT system

The FIBHT system exhibits three main advantages, as depicted in Fig. 1A: high permeability/stretchability, allowing skin to breathe and deform; bioadhesiveness, ensuring a stable skin-electrodes interface;

[1]Department of Biomedical Engineering, City University of Hong Kong, Hong Kong SAR, China. [2]Department of Applied Biology and Chemical Technology, The Hong Kong Polytechnic University, Hong Kong SAR, China. [3]Hong Kong Centre for Cerebro-Cardiovascular Health Engineering (COCHE), Hong Kong Science Park, Hong Kong SAR, China. [4]Department of Materials Science and Engineering, Southern University of Science and Technology, Shenzhen 518055, China. [5]Department of Precision Machinery and Precision Instrumentation, University of Science and Technology of China, Hefei 230026, China. [6]Research Institute for Intelligent Wearable Systems (RI-IWEAR), The Hong Kong Polytechnic University, Hong Kong SAR, China. [7]Research Institute for Smart Energy (RI-RISE), The Hong Kong Polytechnic University, Hong Kong SAR, China. [8]Soft Electronics Research Centre, PolyU-Wenzhou Technology and Innovation Research Institute, Wenzhou, Zhejiang Province, China. [9]The Hong Kong Polytechnic University-Daya Bay Technology and Innovation Research Institute, Huizhou, Guangdong Province, China. [10]Institute of Digital Medicine, City University of Hong Kong, Hong Kong SAR, China.
*Corresponding author. Email: tczzheng@polyu.edu.hk (Z.Z.); xingeyu@cityu.edu.hk (X.Y.)
†These authors contributed equally to this work.
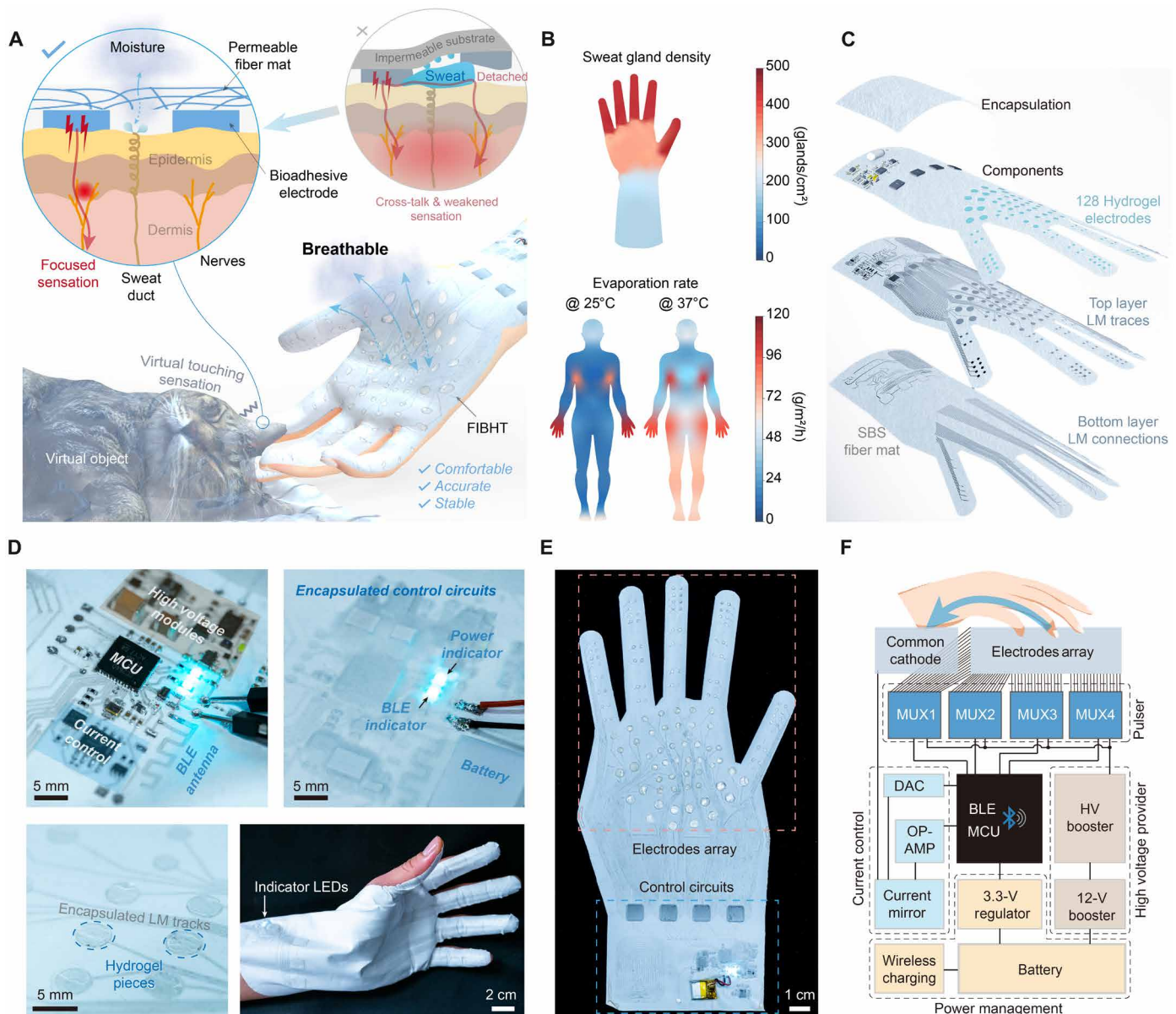
Fig. 1. Schematic illustration of the FIBHT system. (**A**) Conceptual illustration of the features of the FIBHT system. (**B**) Sweat gland density distribution of the hand and sweat evaporation rate distribution on the human body (front) in situations of insensible perspiration (environment, 25°C) and heavy sweating (environment, 37°C). (**C**) Exploded view of the structure of FIBHT. (**D**) Optical image of details in the control circuits both before (left) and after (right) encapsulation. (**E**) Optical image of the complete FIBHT system. (**F**) Brief block diagram of the FIBHT system. DAC, digital-to-analog converter; OP-AMP, operational amplifier.

and a high integration level with high count channels of electrodes, enabling fine, dynamic, and cross-talk–free haptic rendering with high resolution. Permeability matters a lot for wearables on hands, since our hands have the highest perspiration rate (both insensible perspiration and heavily sweating) on the human body (Fig. 1B) (*37*, *50*). The sweat glands on the hand are also substantially denser than other body parts (e.g., wrist and forearm), with the highest density on the fingers (~441 glands/cm²) (*51*). To enhance permeability and flexibility, we adopted SBS fiber as a textile substrate mat with well-patterned LM traces as an electrode that distinguishes FIBHT from the conventional rigid or flexible printed circuit board (fPCB)–based circuits and electronics. The entire FIBHT system was designed and developed in a one

piece with high-level integration, stacking multilayer fashion (Fig. 1C) with LM patterning and encapsulating techniques (fig. S2). Regarding the electronics properties, the functionality of the FIBHT is the same as conventional PCB-based ones, which was validated by programmed light-emitting diode lighting (Fig. 1D and fig. S3). Conductive and bioadhesive hydrogel pieces were placed on top of the LM electrode sites, which can be firmly adhered to the skin, forming a low-impedance electrode-skin interface serving as the electrotactile current pathway that keeps steady without external support and even under deformation.

To realize effective electrotactile feedback with high recognition efficiency, we designed 128 electrode sites over the hand region, where the density and distribution mimic the mechanoreceptors innervation

density and two-point discrimination limen of the human hand (text S2). To deliver stimulation current in all 128 channels, four high-voltage multiplexing switches (MUXs) are deployed to provide programmable electrical pulses for these sites (Fig. 1E). The direct current (DC) high voltage of up to 135 V is generated by a two-stage high-voltage boosting module, which draws energy from a 3.7-V lithium-ion battery. The microcontroller unit (MCU) controls MUXs and current control module to drive monophasic current pulses through the skin to stimulate the mechanoreceptor-associated afferent nerves. With various preprogrammed dynamic electrotactile modes, it is convenient to induce different types of tactile sensations in single or multiple sites simultaneously, or moving patterns in multiple positions sequentially, by simply sending short commands via a Bluetooth low energy (BLE) wireless communication module using a mobile device.

## Characterizations of materials and interfaces

The solid electrical connection between components (chips, resistors, capacitors, etc.) and LM pads/traces is crucial for constructing the multilayer LM circuits and routing. Figure 2A illustrates how the pins of components are soldered to the pads using hybrid LM (hLM) solders [i.e., hLM, partially fluidic and partially oxidized LM (oLM)], which was proven to work well under severe stretching (40, 42). We used stiffness-engineered oLM paste to ensure stable contact with the pins of integrated circuit (IC) chip (Fig. 2B), and an additional layer of the pristine LM on top to ensure good connection even under severe stretching. The pads are stencil printed on top of the thin mask (~20 μm in thickness) that protects LM traces but allows oLM paste to penetrate through for stable electrical contact with traces. The components are fixed at the corresponding positions on this mask layer by glue (fig. S4). Vertical interconnect accesses (VIAs) made of fluidic LM guarantee interlayer connectivity, connecting the top and bottom routing layers through laser-ablated holes in the substrate (~100 μm) (Fig. 2C and fig. S5). The traces routed through VIAs have negligible differences in resistance with those connected directly (Fig. 2D), (<10 ohms even under extreme stretching ~500%) and present small fluctuation within 1 ohm during repeated stretching tests (60% strain and 10, 000 cycles; fig. S6). The shorter length interconnects its own lower resistance, which exhibits good electrical conductivity and a recoverable resistance change within 0.4 ohms under up to 400% strain (Fig. 2E). The durability is also great, which can be up to 10,000 cycles under 60% stretching with only ~0.2-ohm fluctuation (Fig. 2F). The great mechanical property allows the LM circuits to keep surviving under various skin deformations. The LM coating causes only slight changes in the mechanical properties of the SBS mat, where only a marginal decrease in stretchability occurs (from 1009 to 865%) (Fig. 2G).

Sole LM is difficult to serve as the electrodes for effective electrotactile stimulation due to its fluidic nature, poor skin adhesion, and insufficient electron-ion exchanging interface, which would lead to an increased interfacial impedance. In contrast, hydrogel electrodes offer stronger tissue adhesion (52) and lower interfacial impedance owing to the abundant electric double layer (EDL) capacitance for easier passing though of alternative currents (AC) (text S3) (53, 54). For this purpose, we developed a bioadhesive and conductive hydrogel as the LM-skin interface to improve the interfacial properties and deliver effective feedback. It is composed of a double polymer network formed by covalent cross-linking of polyacrylamide (PAAm) and multiple tannic acid (TA)–mediated dynamic interactions, with soluted sodium chloride (NaCl) and sodium citrate in a water-glycerol binary solvent system.

Carefully engineering the composition of the hydrogel (fig. S7) enables the introduction of multiple intermolecular interactions (e.g., hydrogen bonding) within hydrogel, and therefore endows the resultant hydrogel with optimal physicochemical performances (text S4). The hydrogel serves as a bridge for charge transport between the skin and the LM, enabling effective electrical stimulation across the skin-device interface. Moreover, such hydrogel exhibits excellent stretchability and a low swelling ratio that minimizes sweat-induced structure deformation, with moisture permeability comparable to commercial gels (fig. S8) and good biocompatibility and antimicrobial effects (figs. S9 and S10 and text S4) (55–57). Meanwhile, the photocurable hydrogel is highly fluidic before curing, which enables it to be definable into small-scale, high-resolution patterns (minimum size, Φ 0.8 mm; and step size, 0.2 mm; fig. S11). To prepare the LM-skin interface, uncured fluidic hydrogel penetrates through the fibrous network of the protective encapsulation mask, establishing stable electrical contact with the LM through robust interfacial bonding. After in situ ultraviolet (UV) cross-linking, the hydrogel becomes robustly fixed within the skeleton of SBS fiber mat, while the hydrogel/SBS mat/LM composite remains a low modulus of ~120 kPa (Fig. 2H and fig. S12). The LM-hydrogel interface is clearly shown in the scanning electron microscope (SEM) images (Fig. 2I) and the bonding is validated by x-ray photoelectron spectroscopy (XPS) results and contact angle changes in stretching (figs. S13 and S14 and text S5). The low LM-hydrogel interfacial areal impedance is validated by electrochemical impedance spectroscopy test with different hydrogel sizes for adapting different thresholds (fig. S15). The impedance of the electrodes remains low and highly stable in a period of 7 days (fig. S16), indicating that the hydrogel-LM interface will not suffer from severe oxidation of the LM. The reason may be that the TA composition in the hydrogel is a reducing agent (58–60) and prevents the LM from being oxidized, and the low water content (water/glycerol = 4:3) owing to binary solvent system can also slow this process. Owing to functional components like TA and PAAm, strong skin adhesion and robust bonding with LM are achieved through multiple dynamic interactions (e.g., hydrogen bond, Schiff-base/Michael addition reaction, cation-π interaction, and metal coordination) and physical entanglement (e.g., long polymeric chains of PAAm) (Fig. 2K). As a result, the total impedance of the LM-hydrogel-skin interface is significantly lower than that of dry electrodes (i.e., Au) and commercial gel with the same size (Fig. 2L). Even when stretched to 100%, the impedance remains low and allows high maximum current to pass through (fig. S15).
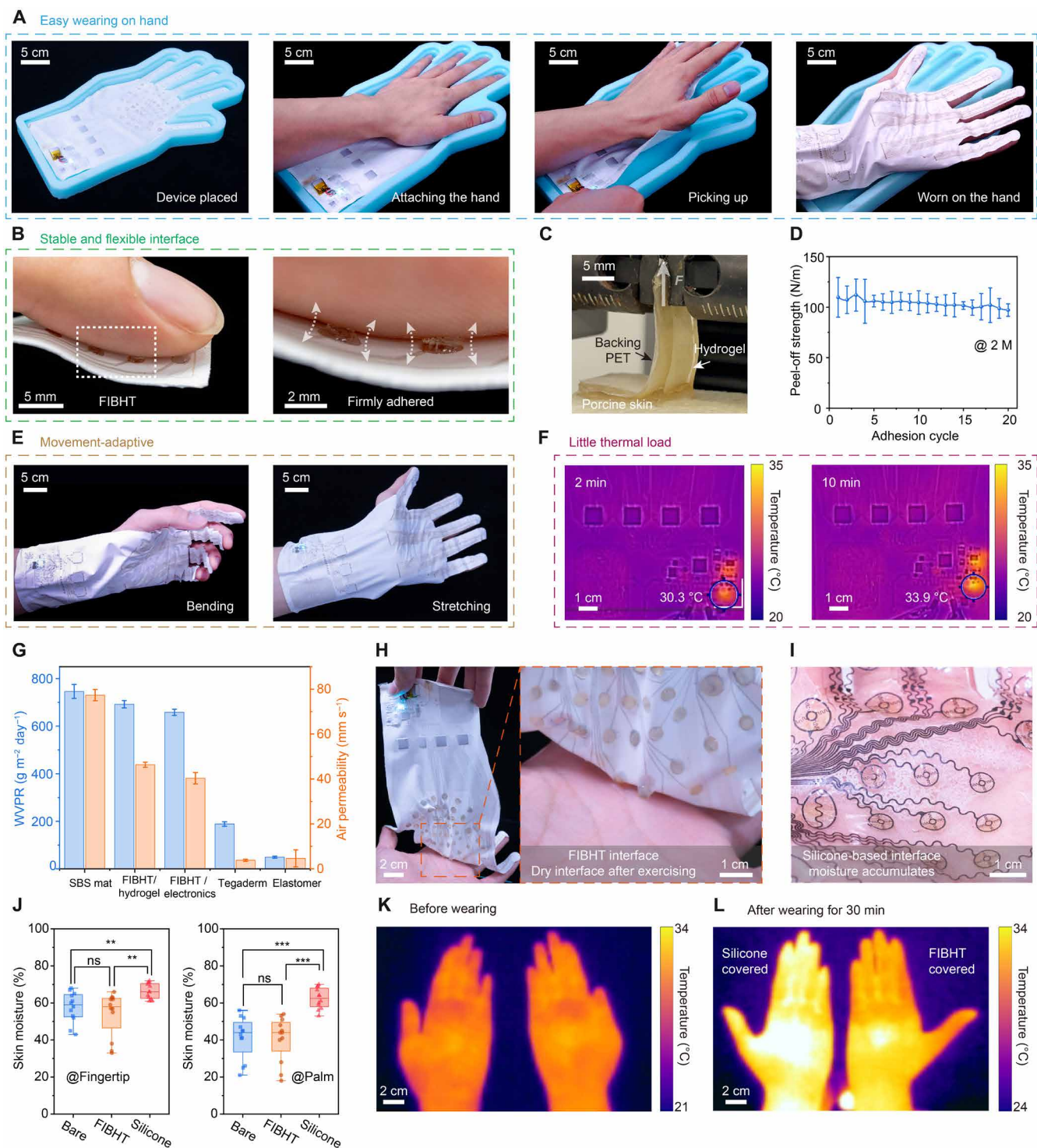
Wearing comfort of the FIBHT

The use of soft, stretchable, and permeable materials substantially enhances the comfortability of the FIBHT compared to those rigid or impermeable devices. The bioadhesive nature of the hydrogel electrodes eliminates the need for additional tape or adhesive, simplifying the wearing process, as the user only needs to attach the hand onto the device and pick it up (Fig. 3A and movie S1). The textile substrate conforms and securely adheres to the hand (Fig. 3B). The peel-off and lap-shear tests verify the exceptional and durable tissue adhesiveness of hydrogel (Fig. 3C and fig. S12), with peel-off strength declining only ~8% after 20 cycles (Fig. 3D). Owing to the ring-shaped architecture of the hydrogel/LM interface and the plasma-strengthened hydrogel-SBS binding strength (fig. S12, G to I), the hydrogel can be securely fixed on the substrate and could also detach from the skin intact when taking off FIBHT (fig. S17). The FIBHT also shows great adaptation to typical deformations of the skin (Fig. 3E). Notably, the electronics generate heat primarily at the high voltage
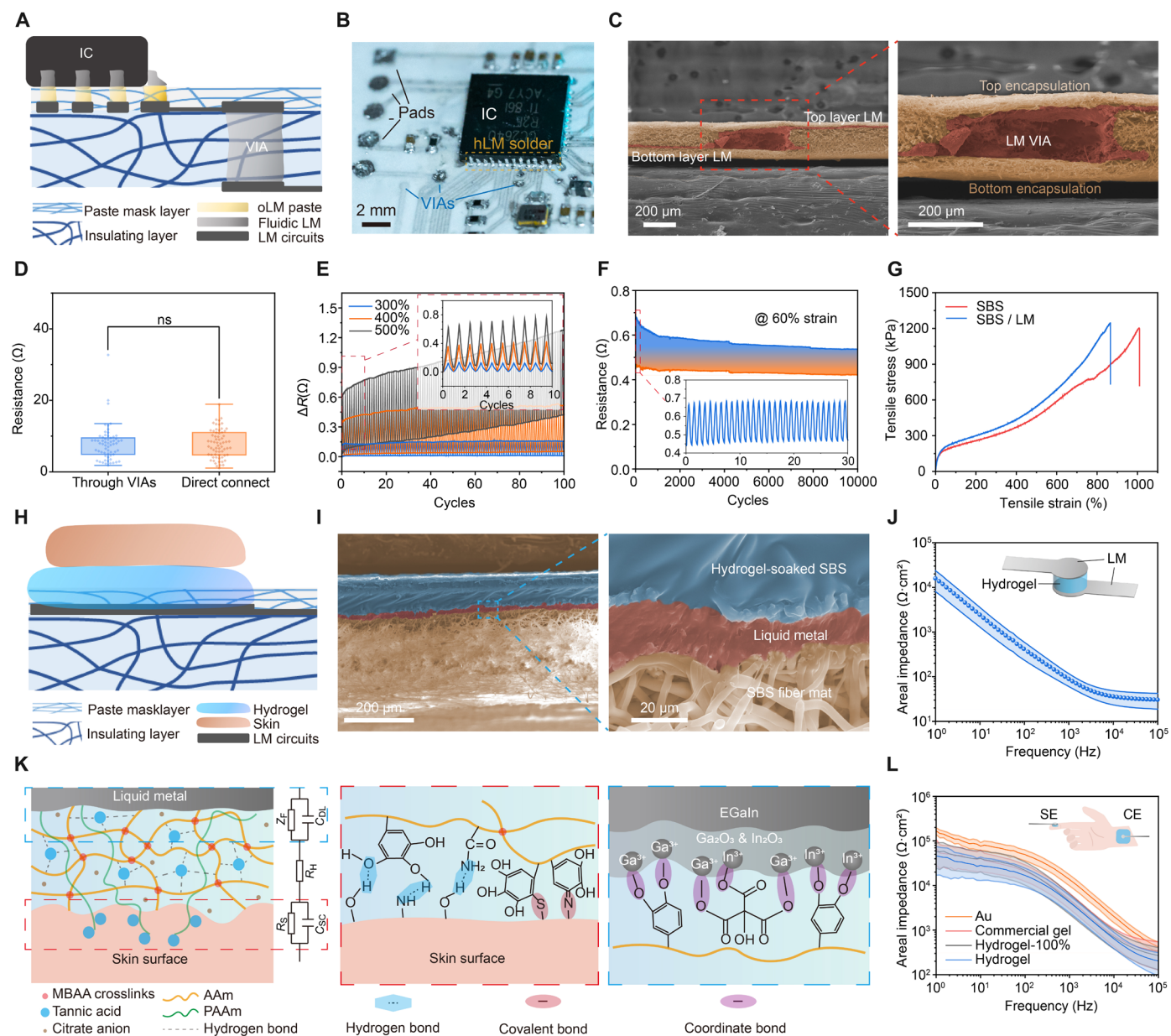
Fig. 2. Structures and materials of the system and interfaces. (**A**) Schematic illustration of the cross-sectional view of the multilayer electronic circuits integration. (**B**) Optical image of the soldered chips and circuit details. (**C**) SEM images of the cross section of the LM VIA. (**D**) Resistance distribution of the LM traces to 128 electrodes, classified by connection through VIAs or direct connect. $n = 62$ for "through VIAs" group and 66 for "direct connect" group. ns, not significant ($P > 0.05$ in t test). (**E**) Resistance changes in extreme stretching test (300, 400, and 500% strain) of the LM trace. Thick line: curve envelopes. Inset: zoomed plot showing the initial 10 cycles. (**F**) Resistance changes in cycled stretching test of the LM trace (length, 5 mm; and width, 254 μm). Inset: zoomed plot showing the initial 30 cycles. (**G**) Stress-strain curves of pristine SBS mat and LM coated SBS. (**H**) Schematic illustration of the cross-sectional view of the skin/hydrogel/LM integration. (**I**) SEM images of the cross section of the hydrogel/LM interface on SBS fiber mat. (**J**) Areal impedances of the LM/hydrogel interface, with three sizes of hydrogel pieces. $n = 9$ (diameters of 2, 4, and 6 mm, three in each group). (**K**) Schematic illustration of the bonding in LM/hydrogel/skin interfaces and their equivalent circuit modal. MBAA, N,N'-methylenebisacrylamide; AAm, acrylamide; Z_F, Faradic impedance; C_{DL}, electric double layer capacitance; R_H, hydrogel access resistance; R_S, skin resistance; C_{SC}, stratum corneum capacitance; EGaIn, eutectic gallium-indium. (**L**) Electrode-skin areal total impedances of bioadhesive hydrogel, 100% stretched hydrogel, commercial gel, and gold (Au) electrodes. $n = 9$ (diameters of 2, 4, and 6 mm, three in each group). SE, stimulating electrode; CE, counter electrode. For (E), (J), and (L), line: mean value. Error band: SD.

boosting modules, with a highest temperature of 33.9°C during steady operation (Fig. 3F) in 10 min. In a long-time heavy-duty operation of 90 min, the highest temperature of the device is ~40° ± 1°C (fig. S18). As the threshold of contact-induced thermal pain is 43° to 45°C (*61*, *62*), the temperature of FIBHT is maintained below this range and will not cause any thermal discomfort.

As the key feature of the FIBHT system, the high permeability allows normal evaporation of moisture and breathability for the covered skin. While the presence of electronic components and hydrogel affects the permeability slightly compared to the pristine SBS mat, it still outperforms medical tape (Tegaderm, 3M) and intact elastomer (e.g., Ecoflex, Smooth-On) thin films in terms of

Fig. 3. Wearing comfortability of the FIBHT. (**A**) Wearing process of the FIBHT. (**B**) Optical images showing the skin adhesion of bioadhesive hydrogel. (**C**) Optical images of the peel-off test. (**D**) Cycled peel-off test results. $n = 3$ for each data point. Error bar: SD. (**E**) Optical images of the FIBHT on the hand during deformation. (**F**) Infrared thermal images showing the temperature distribution of the control circuit when it is working. (**G**) Water vapor penetration rate (WVPR) and air permeability results comparison between various samples. $n = 3$ for each bar. Bar height: mean value. Error bar: SD. (**H** and **I**) Optical images showing the dry interface and the accumulated moisture that condensed in inner surface of silicone-HI, after exercising (30 min). (**J**) Relative skin moisture comparison between bare hands (before wearing), FIBHT, and silicone-HI after wearing for 30 min. $n = 12$; ns, not significant. **$P < 0.01$ and ***$P < 0.001$. Square, mean; center line, median; box limits, upper and lower quartiles; whiskers, 1.5× interquartile range; points, outliers. (**K**) Infrared thermal images showing the hands' temperature in original (before wearing) group and (**L**) after wearing FIBHT (right hand) and silicone-HI (left hand) groups.

water vapor penetration rate (>657 g m^{-2} day^{-1}) and air permeability (>40 mm^{-1} under 100 Pa pressure) (Fig. 3G). This superior permeability proves beneficial in intense sports or hot environments. Following 30 min of slight exercise (jogging) with the FIBHT, the palm remains dry due to moisture evaporation through the fibrous architecture (Fig. 3H). In contrast, the impermeable silicone-based device shows the condensed moisture accumulation in the same condition (Fig. 3I). Measurements of relative skin moisture on both fingertip and palm before and after 30-min of wearing indicate significant increases only in the silicone-covered group (Fig. 3J). Moreover, the FIBHT effectively maintains the hand's skin moisture level and temperature, while impermeable interface makes the user feel hot and disconformable on the hand (Fig. 3, K to L). Although it is moisture permeable, the FIBHT was proven waterproof by rain testing (blotting paper weight added only 0.3 g), owing to the hydrophobicity of the SBS fiber mat (fig. S19 and movie S2).

Dynamic feedback for precise haptic recognition

As mentioned in the introduction, we achieved a high channel number and high density of stimulating electrodes. However, because of the differences of sensitivity (including thresholds and two-point discrimination distance) among people, a high electrodes spatial resolution does not always lead to a high recognizing precision. So here, first, we investigated the static spatial (SS) recognition ability in 12 volunteers (six males and six females). Volunteers were asked to identify the location of feedback among the eight electrodes on the fingertip (Fig. 4A), as the interchannel cross-talk is negligible in this array (fig. S20). For each volunteer, we customized FIBHT with suitable finger length and four different pitch lengths in fingertip electrodes (fig. S21) to make sure it matches the two-point discrimination limen of the volunteer. Testing results showed an overall identification rate of 81.5% (Fig. 4, B and C), slightly higher for electrodes closer to the tip. Gender differences were not significant, but the recognizing ability varied among individuals (Fig. 4D). During testing, sweating was observed to decrease identification accuracy. We selected four volunteers with highest recognition accuracy (>85%) and conducted the test after wearing FIBHT and an impermeable silicone haptic interface (silicone-HI) for 30 min (Fig. 4, E and F). The FIBHT group maintained high accuracy, while the silicone-HI group showed a blurry/vague recognition result (Fig. 4G) after long-term wearing, reflected in decreased identification rate of 53.8% (Fig. 4H). The reason for this decrease could be the increased moisture in silicone-covered skin, which worsens the cross-talk among adjacent channels. Thus, the excellent permeability of FIBHT is crucial for maintaining effective precise feedback in long-term use.

As our goal is to realize clearly recognizable haptic feedback, the study of whether dynamic stimulation could bring a difference is critical, since static feedback always seems to result in a fading sensation with time. Hence, we programmed eight different spatiotemporal patterns for distinguishing (ST 1 to 8; Fig. 4I and fig. S22), where individual channels were sequentially activated. The result shows that the prediction accuracy is improved by changing static feedback into dynamic ones (overall, 89.7%; and worst, 82.5%; Fig. 4J). The statistical results sorted according to individuals show a closer range than in static situations (Fig. 4K), but significant differences could be seen among patterns. As shown in Fig. 4L, patterns ST5 and ST6 result in outstanding identification rates that reach above 96%, featuring simultaneously stimulating with two parallel channels, which could make the perception clearer. Compared to SS feedback, the individual

average identification rates show significant improvements (verified by paired t test; Fig. 4M), which proved that spatiotemporal dynamic feedback provides more information and is much easier to precisely distinguish.

The palm has higher thresholds of two-point discrimination due to the lower innervation density of mechanoreceptors, so, fine patterns of spatiotemporal scanning may not be accurately perceived, and therefore lead to confusion in received information. To enhance the conveyance of tactile information beyond position and strength, we replaced consistent stimulation with encoding information into dynamic cycling temporal stimulation waveforms. For example, for a shorter timescale (≤ 2 s), we developed temporal periodic dynamic modes (TP 1 to 4), which alter the on and off states of stimulation with different periods. However, for longer timescales (2 to 10 s), the perception intensity may fade despite consistent current strength. To address this, we devised temporal fading dynamic modes (TF 1 to 4), featuring gradually increasing pulse intervals, and returning to densely fired pulses at the start of next period (Fig. 4N). This sudden frequency change is clearly perceptible and keeps the sensation refreshed. To assess the sensitivity of different hand regions to temporal patterns, we evaluated five typical positions including fingertip, phalanx, metacarpophalangeal (MCP) joint, hypothenar eminence (HYT), and inner palm. All these dynamic modes were well recognized in all five regions. The overall identification rate reaches 94.2% with the minimum of 90% (Fig. 4O). Besides, every volunteer achieved a high average accuracy of near or above 90% (Fig. 4P), which indicates that temporal dynamic feedback could very precisely convey information to users in general. Analysis of individual TP/TF modes revealed a growing trend of identification rate with increasing period length (Fig. 4Q). In general, dynamic modes with a period length above 1 s could be accurately distinguished (accuracy, >92.5%). This temporal encoding method is universally effective to all hand regions as they all achieved above 92% accuracy and showed no significant interregional differences (Fig. 4R and figs. S23 and S34).
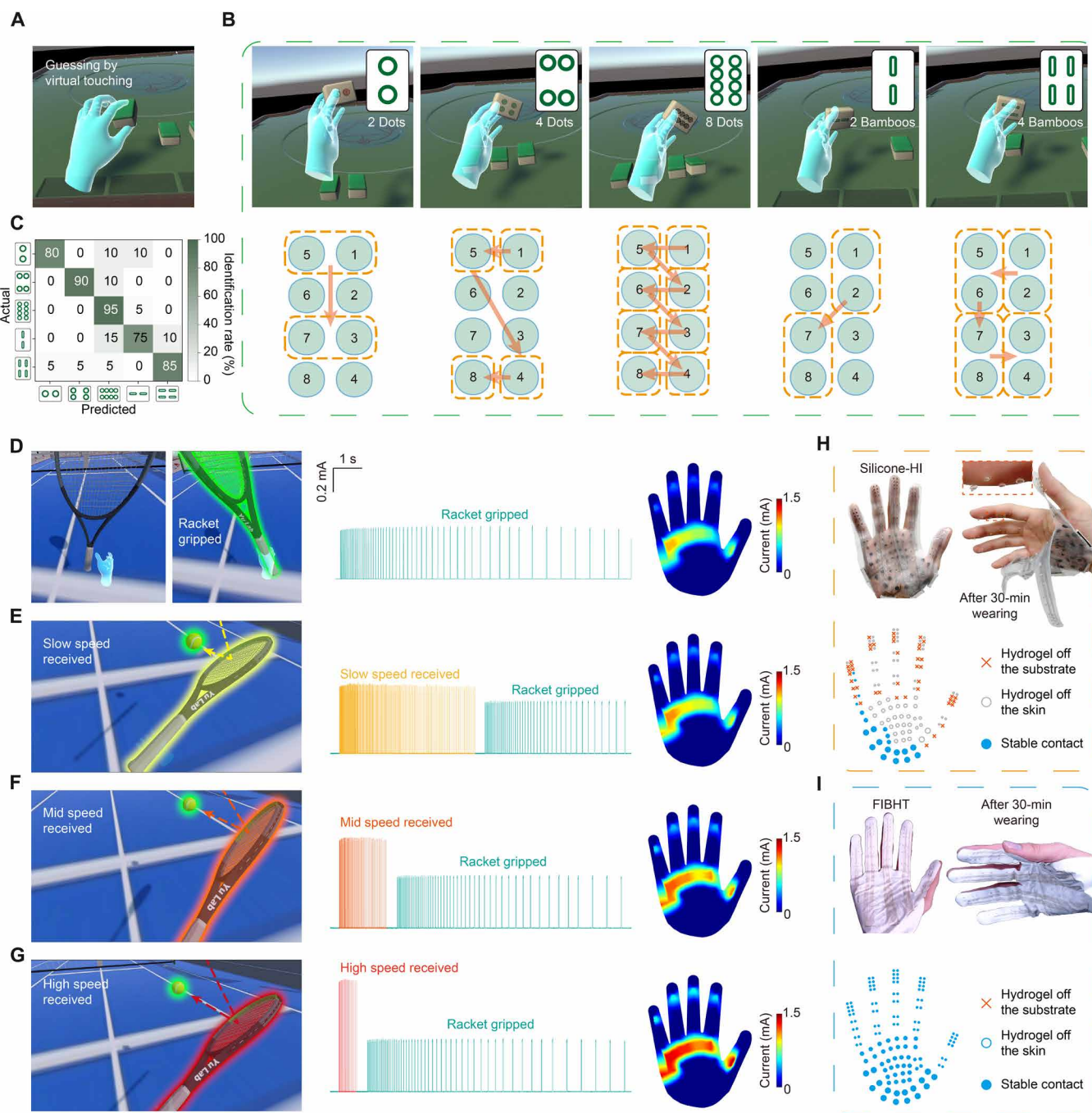
Applications in VR

With the highly recognizable spatiotemporal dynamic feedback modes, we tried to exploit them in achieving better virtual touching and haptic experiences in VR. As the fine patterns could be distinguished on the fingers, FIBHT could greatly assist the object recognition without the visual aids. For example, in a recreational VR game of playing Mahjong, the player picks facing-down tiles on the table. The player tries to recognize the suit and number of the tile using the thumb before flipping it over (Fig. 5A), as it is a common habit in Mahjong players. Here, we designed five types of spatiotemporal patterns for simulating different tiles, including 2 and 4 in Bamboo suit, and 2, 4, and 8 in Dot suit (Fig. 5B and movie S3). Via Bluetooth wireless communication, we synchronized the activation of stimulation pattern with the hand's interaction with tiles, so the player can feel the dynamic pattern on the thumb when picking up one tile without flipping its face upward. The recognizing results show that these Mahjong tiles can be clearly distinguished (Fig. 5C) with this nonvisual, high spatial resolution and dynamic haptic assistance, by incorporating FIBHT in the VR interactions.

Sport games in VR pose a substantial challenge for wearable haptic gloves due to sweat accumulation during intense gaming, resulting in discomfort and deteriorated feedback perception, as the haptic gloves are typically impermeable. FIBHT addresses this challenge by offering the required permeability for VR haptic gloves and thus elevating the player's experience. We customized a VR tennis game, incorporating
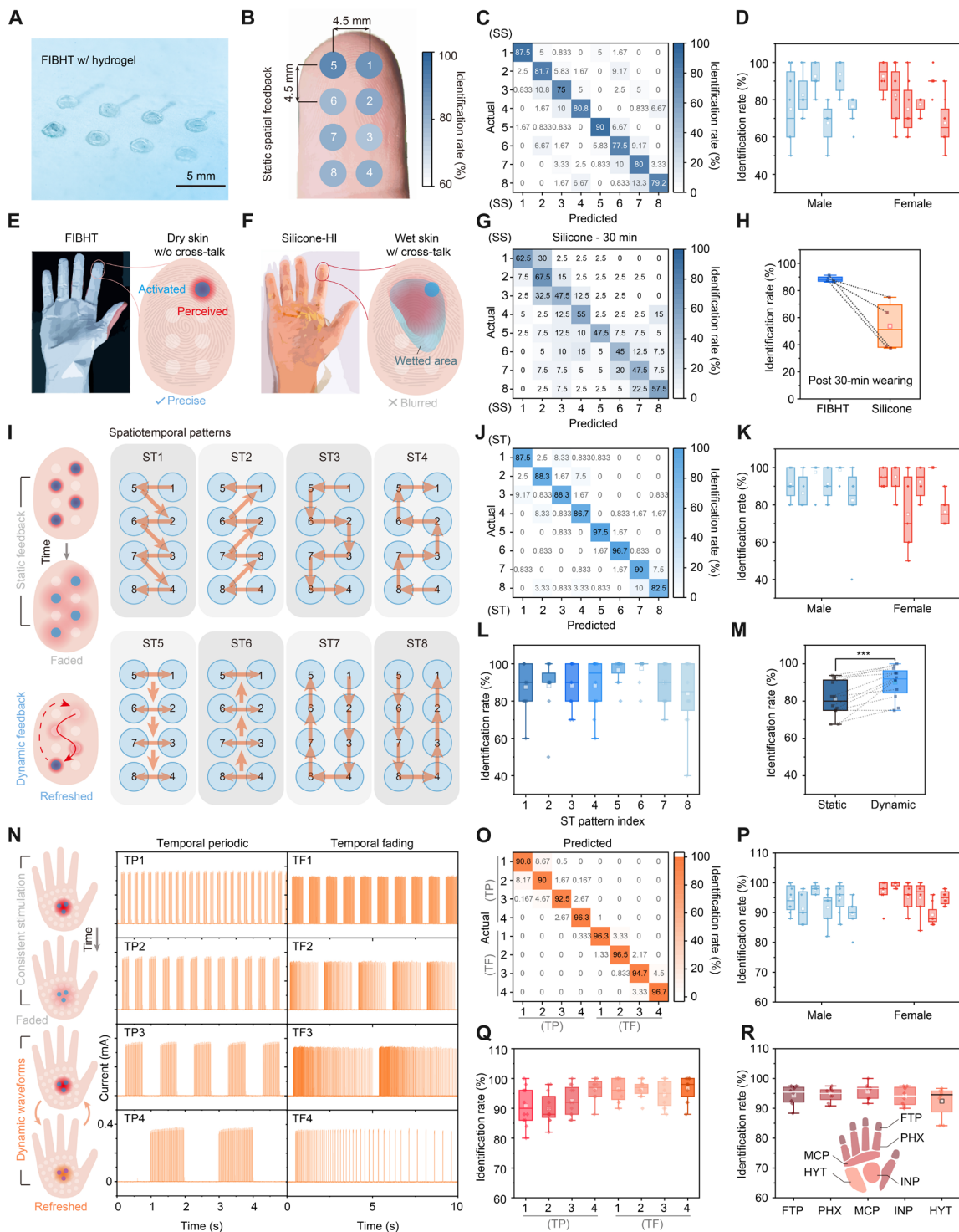
Fig. 4. Dynamic feedback user study. (**A**) Optical image of the eight-channel array on FIBHT for fingertip (FTP) feedback test. (**B**) Overall identification rate distribution on the fingertips. (**C**) Confusion matrix of the static spatial (SS) testing results. (**D**) Identification rate distributions of SS testing in each individual. $n = 8$. (**E** and **F**) Schematic illustration of testing in conditions of wearing FIBHT and silicone-HI for 30 min. (**G**) Confusion matrix of the SS testing results in selected volunteers after wearing silicone-HI for 30 min. (**H**) Comparison of average identification rates between FIBHT and silicone-HI groups. (**I**) Eight different spatiotemporal (ST) dynamic patterns. (**J**) Confusion matrix of the ST testing results. (**K**) Identification rate distributions of ST testing in each individual. $n = 8$. (**L**) Identification rates among ST patterns. $n = 12$. (**M**) Comparison of average identification rates between SS and ST tests. $n = 12$, ***$P < 0.001$. (**N**) Eight different temporal dynamic modes (TP/TF). (**O**) Confusion matrix of the TP/TF testing results. PHX, phalanx; MCP, metacarpophalangeal joint; HYT, hypothenar eminence; INP, inner palm. (**P**) Identification rate distributions of TP/TF testing in each individual. $n = 8$. (**Q**) Identification rates among TP/TF modes. $n = 12$. (**R**) Identification rate distributions of TP/TF testing in five regions of the hand. $n = 8$. For all box plots, square, mean; center line, median; box limits, upper and lower quartiles; whiskers, 1.5× interquartile range; points, outliers.

Fig. 5. Applications of FIBHT in VR. (**A**) Capture of VR scenario where the player is recognizing the Mahjong tile using the thumb without flipping it. (**B**) Five different Mahjong tiles and the corresponding feedback patterns. (**C**) Confusion matrix of identifying these Mahjong tiles (four volunteers, each tile for five times). (**D** to **G**) VR scenarios of a tennis game, corresponding temporal dynamic feedback and the current distributions, including gripping the tennis racket (D), slow speed received (E), mid speed received (F), and high speed received (G). (**H** to **I**) Comparison of working electrodes distributions between wearing silicone-HI (H) and FIBHT (I), both after wearing for 30 min.

various haptic interactions to enhance immersion. Initially, the player grips the virtual racket and simultaneously experiencing a weak, long-period temporal-fading dynamic stimulation on the hand (mainly MCP, upper HYT, and lower part of fingertips; Fig. 5D) to simulate the racket's presence. The gripping sensation varies based on the opponent's ball speed, with faster serves resulting in shorter but stronger contact with the

racket. To distinguish between slow-, medium-, and high-speed serves, we synchronized these scenarios and adjusted the stimulation modes accordingly. For higher-speed serves, we reduced the fading periods and increased the intensity, allowing for a clear distinction (Fig. 5E-G, Movie S4). Consequently, the player can feel the feedback of gripping the racket and hitting the tennis ball in VR, even after extended play and

perspiration. While unbreathable silicone-HI cannot provide stable feedback after wearing for 30-min game playing, because most hydrogels are either detached from the substrate (lacks fixing architecture) or the skin (sweat-caused reducing in adhesion; Fig. 5H), FIBHT keeps all electrodes tightly adhered to the hand, which guarantees the stable feedback experience (Fig. 5I and movie S5).

DISCUSSION

Being thin, soft, and wirelessly operable are important factors for haptic wearables, while another important quality that is essential to haptic wearables is to make the user feel comfortable, which requires the wearable be breathable while staying firmly adhered to the skin. In this work, we developed a FIBHT with optimized design (text S6) to realize all these purposes, exhibiting great stretchability, precise dynamic rendering ability, and wireless features, which provides a paradigm-shift solution to the new generation of haptic interfaces. Through comprehensive material/device characterizations and user studies, coupled with interaction with VR, we demonstrate the potential of the FIBHT as a comfortable and high-performance haptic interface. Compared with other works of haptic interfaces and our prior works, the FIBHT has superior comprehensive performances in breathability, stretchability, interfacial adhesive properties, stability, electrodes number/pixel density, monolithic system integration, sweat-insensitive high recognition precision, etc. The technologies reported in this work bridge the gap between virtual objects and our skin's sensory perception without external constraints or hindrance to skin respiration, thereby paving the way for better immersive experiences. We believe that the current demonstrations cannot fully reveal the FIBHT's potential in more universal scenarios. Through the integration with artificial intelligence–based backend analysis and closed-loop feedback parameters adjustments, this technology could possibly become a faithful "haptic media" between humans and anything that needs to be touched but they are unable to, no matter for VR players, patients with neural disease, teleoperators of robotics, or anyone.

MATERIALS AND METHODS
Materials
All processing solvents were used as received. LM, euthetic GaIn, (melting point 15.7°C, Sigma-Aldrich), and SBS (Kraton) were used as received. Sodium chloride (NaCl, Macklin), sodium citrate (Macklin), glycerol (Macklin), PAAm (with an average molecular weight of 500 million, Macklin), TA (Sigma-Aldrich), acrylamide (AAm, Macklin), and lithium phenyl-2,4,6-trimethylbenzoylphosphinate (LAP, Yinchang New Materials Co. Ltd., Shanghai, China) were used as received. NIH/3T3 cell lines (ATCC CRL-1658) were obtained from the Cell Bank of the Chinese Academy of Sciences (Beijing, China). Phosphate-buffered saline, Dulbecco's minimum Eagle medium, fetal bovine serum, and penicillin/streptomycin were purchased from Gibco, Hong Kong.

Fabrication
The fabrication of FIBHT begins with electrospinning a layer of SBS fiber mat (~100 μm) as the substrate for supporting top and bottom layers of LM traces on both sides. The polymer solution was prepared by dissolving the SBS polymer with a weight ratio of 13 wt % in the mixed solvent (tetrahydrofuran/dimethylformamide = 3:1). The

voltage was set as 18 kV and the collecting distance was 15 cm. Then, the top layer LM (traces, antennas, footprints of ICs or other components, headers, etc.) was patterned by using thin-film stencil printing. First, a SBS fiber mat (~100 μm) was prepared by electrospinning, which serves as the substrate. The polymer solution for electrospinning was prepared by dissolving the solution SBS (Kraton) with a weight ratio of 14 wt % in the mixed solvent (weight ratio of tetrahydrofuran/dimethylformamide = 3:1). The voltage was set as 18 kV, the feeding rate was 4 ml/hour, and the collecting distance was 15 cm. Then, both sides of it were covered seamlessly with thin polyimide (PI) films (thickness, ~25 μm). Next, the board outline and VIAs were drilled in all three layers by laser cutting system (ProtoLaser U4, LPKF Laser & Electronics SE) with high-power laser, then followed by laser defining of the top PI stencil alone with low power laser. Then, LM was stencil printed onto the substrate serving as the bottom layer traces, and stencil was removed. Another SBS fiber mat (~20 μm) was additively electrospun onto the LM circuits as the bottom encapsulation. Then, it is flipped over, and the top layer LM was patterned on the back side of the substrate in the same way, followed by electrospinning another SBS fiber mat on it as the protective mask (~20 μm). Then, stiff oLM (pristine LM treated in 80°C for 16 hours) was stencil printed (laser-cut PI film, 25 μm) on the protective mask of the circuit part as the pads and paste for the paste mask layer, which penetrated through the ultrathin mask and contacts with the bonding sites of the top layer LM. The components were placed on the corresponding pads and fixed in position with the aid of glue. With the electrical connection between pad and every pin of components all secured by applying hLM solder on it (weight ratio of oLM/LM is 1:2), and the entire system proved to work properly, a top encapsulation layer of SBS fiber mat (~50 μm) was subsequently electrospun onto the circuits. Last, the outline of FIBHT was tailored by laser cutting.

The hydrogel was prepared by first dissolving sodium chloride (NaCl) and sodium citrate into water-glycerol binary solvent system, followed by adding and mixing PAAm, TA, and AAm. After constant stirring overnight, bioadhesive hydrogel precursor solution was obtained by introduction of MBAA and LAP. The specific components for preparing bioadhesive hydrogel and their dosages are listed in table S2. Then, the uncross-linked hydrogel precursor was poured into the laser-cut thin silicone mold on a clean glass sheet. With UV irradiation for ~1 min, the hydrogel was cross-linked and cured in desired shapes. In FIBHT fabrication, the mold is placed on the electrodes part of FIBHT with patterns aligned, followed by pouring hydrogel precursor and curing it by UV. After curing, the mold is peeled off, leaving the hydrogel patches on 128 sites of the electrodes array and the whole fabrication of FIBHT finishes.

Characterizations
The voltage and current data were measured by a data acquisition system (DAQ 6510, Keithley) with a sampling rate of 60 kHz. The resistances of LM routings were measured by four-terminal method with a source meter (Keithley 2400) coupled with a customized stretching machine (Zolix). The morphology and structures images were taken by SEM (TESCAN VEGA3) and XPS (Thermo Fisher Scientific Xesa). The tensile testing, peel-off testing, and lap-shear testing were conducted using Instron 5942 Micro Tester. The impedances of LM/hydrogel interface and electrode-skin interface were measured by an electrochemical workstation (CHI 660e, CH Instruments). The Fourier transform infrared (FTIR) spectroscopy was

tested using FTIR spectrometer (PerkinElmer Spectrum Two, USA). The temperature characterization was conducted by thermal imaging using a handheld infrared thermal camera (FLIR C5). The skin moisture was measured by a handheld skin tester (Real Bubee RBX-916). The air permeability tests were conducted using a MO21S air permeability tester (SDL Americ Inc.) under the ASTM D737-08 standard (airflow pressure, 100 Pa). Moisture permeability tests were performed by the cup method under the standard E96/E96M-13 (duration, 48 hours). The temperature (22°C) and humidity (63%) were kept constant during all permeability tests. The standard rain test was conducted according to AATCC Test Method 35-2006, with a water spraying duration of 2 min. All optical photos were taken by a digital camera (Sony A6400).

Electronic system

The circuit design was completed by using EasyEDA. The Bluetooth-embedded MCU (CC2640R2F, Texas Instruments) is deployed as the central controller for the whole system. The MCU is programmed using Code Composer Studio (Texas Instruments). A low-dropout regulator (TPS76933, Texas Instrument) provides a stable 3.3 V power supply for MCU. A two-stage high-voltage boosting module (LT8364 & LT8331, Analog Devices) is used for providing the DC high voltage. Four 32-channel analog switches (HV2801, Microchip) are used as the multiplexer for 128 stimulating channels and a pulse modulator. To precisely control the current intensity, a current mirror is deployed using dual-chip transistors (FFB5551, ON Semiconductor). Its reference current is controlled by the analog signal from a digital-to-analog converter (DAC60502, Texas Instruments). The actual current signal is monitored by measuring the voltage between a fixed resistor with a voltage follower (LM258, Texas Instruments). By a customized Android app (composed by Android Studio 2022.2.1), the control of stimulating channels, electrical parameters, and monitoring of actual currents can be realized with wireless BLE communication and operated conveniently on the graphical user interface.

VR system

The Oculus Quest VR headset (Meta) was used to deliver VR visuals to the user, while its hand-tracking functionality was activated to monitor the spatial location, orientation, and gestures of the user's hands. The three-dimensional (3D) VR environment presented to the user via Oculus Quest was generated using Unity3D (version 2020.3.28f1) on a computer. Hand-tracking data were transmitted back to Unity3D, and the interaction between Oculus Quest and the computer was facilitated through Oculus Link. Within the Unity3D environment, initial script execution involved the transmission of current, stimulation frequency, and duty cycle settings to the FIBHT system via BLE. The Unity3D produced collision detection points on a hand model and will compute the penetration depths between the collision detection points and the collider of a designated 3D object. Upon contact between the collision detection points and the collider, penetration depths exceed zero and trigger feedback. Different stimulation patterns are assigned to different objects or scenarios, and corresponding commands were then dispatched to the FIBHT system via BLE to administer the appropriate tactile feedback pattern to the user. Conversely, when the collision detection points and the collider were not in contact, resulting in penetration depths of zero, cessation commands were transmitted to the FIBHT system to halt stimulation.

Haptic recognition user study

We recruited 12 volunteers (including six males and six females, ages 22 to 32) for the user study. They are required to wear the FIBHT on one of their hands to perceive the programmed feedback and tell which site or dynamic patterns are triggered to stimulate the hand. The volunteers are blinded about the actual stimulation sites/patterns. Specifically, there are three groups of testing, SS, spatiotemporal dynamic (ST), and temporal dynamic (TF/TP). In each group, there are eight different sites or dynamic modes (patterns), and each one was randomly repeated 10 times. Basically, monophasic stimulating currents with fixed frequency and duty cycle (50 Hz, 5%) were applied. The SS and ST groups are conducted on eight electrodes on the fingertip, where the mechanoreceptor innervation is densest and has the highest spatial recognizing resolution on the hand. The center-to-center distances of every two electrodes were fixed at 4.5 mm, while the current intensity was set according to the user's individual threshold. The TF/TP group is independently conducted in five different regions on the hand (fingertip, phalanx, MCP joint, inner palm, and hypothenar eminence). The period length of each dynamic mode is listed as follows: TP1: 0.2 s, TP2: 0.5 s, TP3: 1 s, TP4: 2 s, TF1: 1 s, TF2: 2 s, TF3: 5 s, and TF4: ~10 s. In each group of testing, the volunteers were allowed to pick their preferred hand, finger, or site of each position for testing. The testing on volunteers was performed with their full, informed consent. All human experiments were performed in accordance with protocols approved by the Human Subjects Ethics Sub-Committee of Research Committee, City University of Hong Kong, Hong Kong, China [Result of Research Ethics Review Application (Human Research)-(HU-STA-00000850)] and conducted in compliance with the guidelines.

Supplementary Materials

The PDF file includes:
Texts S1 to S6
Tables S1 and S2
Figs. S1 to S34
Legends for movies S1 to S5
References

Other Supplementary Material for this manuscript includes the following:
Movies S1 to S5

REFERENCES AND NOTES

1. A. B. Vallbo, R. S. Johansson, Properties of cutaneous mechanoreceptors in the human hand related to touch sensation. *Hum. Neurobiol.* **3**, 3–14 (1984).
2. Y. Huang, K. Yao, J. Li, D. Li, H. Jia, Y. Liu, C. K. Yiu, W. Park, X. Yu, Recent advances in multi-mode haptic feedback technologies towards wearable interfaces. *Mater. Today Phys.* **22**, 100602 (2022).
3. Y. H. Jung, J.-H. Kim, J. A. Rogers, Skin-integrated vibrohaptic interfaces for virtual and augmented reality. *Adv. Funct. Mater.* **31**, 2008805 (2021).
4. D.-H. Kim, N. Lu, R. Ma, Y.-S. Kim, R.-H. Kim, S. Wang, J. Wu, S. M. Won, H. Tao, A. Islam, K. J. Yu, T. Kim, R. Chowdhury, M. Ying, L. Xu, M. Li, H.-J. Chung, H. Keum, M. McCormick, P. Liu, Y.-W. Zhang, F. G. Omenetto, Y. Huang, T. Coleman, J. A. Rogers, Epidermal electronics. *Science* **333**, 838–843 (2011).
5. Y. Zhao, B. Wang, J. Tan, H. Yin, R. Huang, J. Zhu, S. Lin, Y. Zhou, D. Jelinek, Z. Sun, K. Youssef, L. Voisin, A. Horrillo, K. Zhang, B. M. Wu, H. A. Coller, D. C. Lu, Q. Pei, S. Emaminejad, Soft strain-insensitive bioelectronics featuring brittle materials. *Science* **378**, 1222–1227 (2022).
6. Y. Jiang, S. Ji, J. Sun, J. Huang, Y. Li, G. Zou, T. Salim, C. Wang, W. Li, H. Jin, J. Xu, S. Wang, T. Lei, X. Yan, W. Y. X. Peh, S.-C. Yen, Z. Liu, M. Yu, H. Zhao, Z. Lu, G. Li, H. Gao, Z. Liu, Z. Bao, X. Chen, A universal interface for plug-and-play assembly of stretchable devices. *Nature* **614**, 456–462 (2023).

7. T. Someya, Z. Bao, G. G. Malliaras, The rise of plastic bioelectronics. *Nature* **540**, 379–385 (2016).

8. H. Hu, H. Huang, M. Li, X. Gao, L. Yin, R. Qi, R. S. Wu, X. Chen, Y. Ma, K. Shi, C. Li, T. M. Maus, B. Huang, C. Lu, M. Lin, S. Zhou, Z. Lou, Y. Gu, Y. Chen, Y. Lei, X. Wang, R. Wang, W. Yue, X. Yang, Y. Bian, J. Mu, G. Park, S. Xiang, S. Cai, P. W. Corey, J. Wang, S. Xu, A wearable cardiac ultrasound imager. *Nature* **613**, 667–675 (2023).

9. W. Gao, S. Emaminejad, H. Y. Y. Nyein, S. Challa, K. Chen, A. Peck, H. M. Fahad, H. Ota, H. Shiraki, D. Kiriya, D.-H. Lien, G. A. Brooks, R. W. Davis, A. Javey, Fully integrated wearable sensor arrays for multiplexed in situ perspiration analysis. *Nature* **529**, 509–514 (2016).

10. D. Jung, C. Lim, H. J. Shim, Y. Kim, C. Park, J. Jung, S. I. Han, S.-H. Sunwoo, K. W. Cho, G. D. Cha, D. C. Kim, J. H. Koo, J. H. Kim, T. Hyeon, D.-H. Kim, Highly conductive and elastic nanomembrane for skin electronics. *Science* **373**, 1022–1026 (2021).

11. W. Yang, S. Lin, W. Gong, R. Lin, C. Jiang, X. Yang, Y. Hu, J. Wang, X. Xiao, K. Li, Y. Li, Q. Zhang, J. S. Ho, Y. Liu, C. Hou, H. Wang, Single body-coupled fiber enables chipless textile electronics. *Science* **384**, 74–81 (2024).

12. Y. Liu, C. Yiu, H. Jia, T. Wong, K. Yao, Y. Huang, J. Zhou, X. Huang, L. Zhao, D. Li, M. Wu, Z. Gao, J. He, E. Song, X. Yu, Thin, soft, garment-integrated triboelectric nanogenerators for energy harvesting and human machine interfaces. *EcoMat* **3**, e12123 (2021).

13. J. Xue, Y. Zou, Y. Deng, Z. Li, Bioinspired sensor system for health care and human-machine interaction. *EcoMat* **4**, e12209 (2022).

14. J. Qi, F. Gao, G. Sun, J. C. Yeo, C. T. Lim, HaptGlove—Untethered pneumatic glove for multimode haptic feedback in reality–Virtuality continuum. *Adv. Sci.* **10**, 2301044 (2023).

15. X. Yu, Z. Xie, Y. Yu, J. Lee, A. Vazquez-Guardado, H. Luan, J. Ruban, X. Ning, A. Akhtar, D. Li, B. Ji, Y. Liu, R. Sun, J. Cao, Q. Huo, Y. Zhong, C. Lee, S. Kim, P. Gutruf, C. Zhang, Y. Xue, Q. Guo, A. Chempakasseril, P. Tian, W. Lu, J. Jeong, Y. Yu, J. Cornman, C. Tan, B. Kim, K. Lee, X. Feng, Y. Huang, J. A. Rogers, Skin-integrated wireless haptic interfaces for virtual and augmented reality. *Nature* **575**, 473–479 (2019).

16. Y. Liu, C. Yiu, Z. Song, Y. Huang, K. Yao, T. Wong, J. Zhou, L. Zhao, X. Huang, S. K. Nejad, M. Wu, D. Li, J. He, X. Guo, J. Yu, X. Feng, Z. Xie, X. Yu, Electronic skin as wireless human-machine interfaces for robotic VR. *Sci. Adv.* **8**, eabl6700 (2022).

17. Y. Liu, C. K. Yiu, Z. Zhao, S. Liu, X. Huang, W. Park, J. Su, J. Zhou, T. H. Wong, K. Yao, L. Zhao, Y. Huang, J. Li, P. Fan, B. Zhang, Y. Dai, Z. Yang, Y. Li, X. Yu, Skin-integrated haptic interfaces enabled by scalable mechanical actuators for virtual reality. *IEEE Internet Things J.* **10**, 653–663 (2023).

18. D. Li, J. Zhou, K. Yao, S. Liu, J. He, J. Su, Q. Qu, Y. Gao, Z. Song, C. Yiu, C. Sha, Z. Sun, B. Zhang, J. Li, L. Huang, C. Xu, T. H. Wong, X. Huang, J. Li, R. Ye, L. Wei, Z. Zhang, X. Guo, Y. Dai, Z. Xie, X. Yu, Touch IoT enabled by wireless self-sensing and haptic-reproducing electronic skin. *Sci. Adv.* **8**, eade2450 (2022).

19. D. Li, J. He, Z. Song, K. Yao, M. Wu, H. Fu, Y. Liu, Z. Gao, J. Zhou, L. Wei, Z. Zhang, Y. Dai, Z. Xie, X. Yu, Miniaturization of mechanical actuators in skin-integrated electronics for haptic interfaces. *Microsyst. Nanoeng.* **7**, 85 (2021).

20. Y. H. Jung, J.-Y. Yoo, A. Vázquez-Guardado, J.-H. Kim, J.-T. Kim, H. Luan, M. Park, J. Lim, H.-S. Shin, C.-J. Su, R. Schloen, J. Trueb, R. Avila, J.-K. Chang, D. S. Yang, Y. Park, H. Ryu, H.-J. Yoon, G. Lee, H. Jeong, J. U. Kim, A. Akhtar, J. Cornman, T. Kim, Y. Huang, J. A. Rogers, A wireless haptic interface for programmable patterns of touch across large areas of the skin. *Nat. Electron.* **5**, 374–385 (2022).

21. Z. Sun, Z. Zhang, C. Lee, A skin-like multimodal haptic interface. *Nat. Electron.* **6**, 941–942 (2023).

22. K. Yao, J. Zhou, Q. Huang, M. Wu, C. K. Yiu, J. Li, X. Huang, D. Li, J. Su, S. Hou, Y. Liu, Y. Huang, Z. Tian, J. Li, H. Li, R. Shi, B. Zhang, J. Zhu, T. H. Wong, H. Jia, Z. Gao, Y. Gao, Y. Zhou, W. Park, E. Song, M. Han, H. Zhang, J. Yu, L. Wang, W. J. Li, X. Yu, Encoding of tactile information in hand via skin-integrated wireless haptic interface. *Nat. Mach. Intell.* **4**, 893–903 (2022).

23. A. Akhtar, J. Sombeck, B. Boyce, T. Bretl, Controlling sensation intensity for electrotactile stimulation in human-machine interfaces. *Sci. Robot.* **3**, eaap9770 (2018).

24. Y. Shi, F. Wang, J. Tian, S. Li, E. Fu, J. Nie, R. Lei, Y. Ding, X. Chen, Z. L. Wang, Self-powered electro-tactile system for virtual tactile experiences. *Sci. Adv.* **7**, eabe2943 (2021).

25. Y. Suga, M. Miyakami, I. Mizoguchi, H. Kajimoto, "3D shape presentation by combination of force feedback and electro-tactile stimulation," in *2023 IEEE World Haptics Conference (WHC)* (IEEE, 2023), pp. 361–367. https://ieeexplore.ieee.org/abstract/document/10224481/references#references.

26. B. Xu, A. Akhtar, Y. Liu, H. Chen, W.-H. Yeo, S. I. Park, B. Boyce, H. Kim, J. Yu, H.-Y. Lai, S. Jung, Y. Zhou, J. Kim, S. Cho, Y. Huang, T. Bretl, J. A. Rogers, An epidermal stimulation and sensing platform for sensorimotor prosthetic control, management of lower back exertion, and electrical muscle activation. *Adv. Mater.* **28**, 4462–4471 (2016).

27. A. Withana, D. Groeger, J. Steimle, "Tacttoo: A thin and feel-through tattoo for on-skin tactile output" in *Proceedings of the 31st Annual ACM Symposium on User Interface Software and Technology* (Association for Computing Machinery, New York, NY, USA, 2018; UIST '18), pp. 365–378.

28. M. Ying, A. P. Bonifas, N. Lu, Y. Su, R. Li, H. Cheng, A. Ameen, Y. Huang, J. A. Rogers, Silicon nanomembranes for fingertip electronics. *Nanotechnology* **23**, 344004 (2012).

29. G. Gu, N. Zhang, H. Xu, S. Lin, Y. Yu, G. Chai, L. Ge, H. Yang, Q. Shao, X. Sheng, X. Zhu, X. Zhao, A soft neuroprosthetic hand providing simultaneous myoelectric control and tactile feedback. *Nat. Biomed. Eng.* **7**, 589–598 (2023).

30. Z. Zhang, Z. Xu, L. Emu, P. Wei, S. Chen, Z. Zhai, L. Kong, Y. Wang, H. Jiang, Active mechanical haptics with high-fidelity perceptions for immersive virtual reality. *Nat. Mach. Intell.* **5**, 643–655 (2023).

31. M. Smith, V. Cacucciolo, H. Shea, Fiber pumps for wearable fluidic systems. *Science* **379**, 1327–1332 (2023).

32. J. Oh, J. Kim, S. Lee, S. Jeong, S. H. Ko, J. Bae, A liquid metal based multimodal sensor and haptic feedback device for thermal and tactile sensation generation in virtual reality. *Adv. Funct. Mater.* **31**, 2007772 (2021).

33. R. L. Peiris, Y.-L. Feng, L. Chan, K. Minamizawa, "ThermalBracelet: Exploring thermal haptic feedback around the wrist," in *Proceedings of the 2019 CHI Conference on Human Factors in Computing Systems* (Association for Computing Machinery, New York, NY, USA, 2019); *CHI '19*, pp. 1–11.

34. Y. Huang, J. Zhou, P. Ke, X. Guo, C. K. Yiu, K. Yao, S. Cai, D. Li, Y. Zhou, J. Li, T. H. Wong, Y. Liu, L. Li, Y. Gao, X. Huang, H. Li, J. Li, B. Zhang, Z. Chen, H. Zheng, X. Yang, H. Gao, Z. Zhao, X. Guo, E. Song, H. Wu, Z. Wang, Z. Xie, K. Zhu, X. Yu, A skin-integrated multimodal haptic interface for immersive tactile feedback. *Nat. Electron.* **6**, 1020–1031 (2023).

35. H. Zhai, H. I. Maibach, Skin occlusion and irritant and allergic contact dermatitis: An overview. *Contact Dermatitis* **44**, 201–206 (2001).

36. B. Zhang, J. Li, J. Zhou, L. Chow, G. Zhao, Y. Huang, Z. Ma, Q. Zhang, Y. Yang, C. K. Yiu, J. Li, F. Chun, X. Huang, Y. Gao, P. Wu, S. Jia, H. Li, D. Li, Y. Liu, K. Yao, R. Shi, Z. Chen, B. L. Khoo, W. Yang, F. Wang, Z. Zheng, Z. Wang, X. Yu, A three-dimensional liquid diode for soft, integrated permeable electronics. *Nature* **628**, 84–92 (2024).

37. S. J. Park, T. Tamura, Distribution of evaporation rate on human body surface. *Ann. Physiol. Anthropol.* **11**, 593–609 (1992).

38. J. Kaiser, A. D. Nimbarte, D. Davari, B. Gopalakrishnan, X. He, Study of skin conductance and perceived discomfort of the hand/finger system under controlled atmospheric conditions. *Theor. Issues Ergon. Sci.* **18**, 442–454 (2017).

39. Z. Ma, Q. Huang, Q. Xu, Q. Zhuang, X. Zhao, Y. Yang, H. Qiu, Z. Yang, C. Wang, Y. Chai, Z. Zheng, Permeable superelastic liquid-metal fibre mat enables biocompatible and monolithic stretchable electronics. *Nat. Mater.* **20**, 859–868 (2021).

40. Q. Zhuang, K. Yao, M. Wu, Z. Lei, F. Chen, J. Li, Q. Mei, Y. Zhou, Q. Huang, X. Zhao, Y. Li, X. Yu, Z. Zheng, Wafer-patterned, permeable, and stretchable liquid metal microelectrodes for implantable bioelectronics with chronic biocompatibility. *Sci. Adv.* **9**, eadg8602 (2023).

41. Z. Huang, Y. Hao, Y. Li, H. Hu, C. Wang, A. Nomoto, T. Pan, Y. Gu, Y. Chen, T. Zhang, W. Li, Y. Lei, N. Kim, C. Wang, L. Zhang, J. W. Ward, A. Maralani, X. Li, M. F. Durstock, A. Pisano, Y. Lin, S. Xu, Three-dimensional integrated stretchable electronics. *Nat. Electron.* **1**, 473–480 (2018).

42. Q. Zhuang, K. Yao, C. Zhang, X. Song, J. Zhou, Y. Zhang, Q. Huang, Y. Zhou, X. Yu, Z. Zheng, Permeable, three-dimensional integrated electronic skins with stretchable hybrid liquid metal solders. *Nat. Electron.* **7**, 598–609 (2024).

43. J. C. Yeo, Z. Liu, Z.-Q. Zhang, P. Zhang, Z. Wang, C. T. Lim, Wearable mechanotransduced tactile sensor for haptic perception. *Adv. Mater. Technol.* **2**, 1700006 (2017).

44. M. D. Dickey, R. C. Chiechi, R. J. Larsen, E. A. Weiss, D. A. Weitz, G. M. Whitesides, Eutectic gallium-indium (EGaIn): A liquid metal alloy for the formation of stable structures in microchannels at room temperature. *Adv. Funct. Mater.* **18**, 1097–1104 (2008).

45. K. Nan, S. Babaee, W. W. Chan, J. L. P. Kuosmanen, V. R. Feig, Y. Luo, S. S. Srinivasan, C. M. Patterson, A. M. Jebran, G. Traverso, Low-cost gastrointestinal manometry via silicone–liquid-metal pressure transducers resembling a quipu. *Nat. Biomed. Eng.* **6**, 1092–1104 (2022).

46. F. Chen, Q. Zhuang, Y. Ding, C. Zhang, X. Song, Z. Chen, Y. Zhang, Q. Mei, X. Zhao, Q. Huang, Z. Zheng, Wet-adaptive electronic skin. *Adv. Mater.* **35**, 2305630 (2023).

47. C. Wang, X. Chen, L. Wang, M. Makihata, H.-C. Liu, T. Zhou, X. Zhao, Bioadhesive ultrasound for long-term continuous imaging of diverse organs. *Science* **377**, 517–523 (2022).

48. H. Choi, Y. Kim, S. Kim, H. Jung, S. Lee, K. Kim, H.-S. Han, J. Y. Kim, M. Shin, D. Son, Adhesive bioelectronics for sutureless epicardial interfacing. *Nat. Electron.* **6**, 779–789 (2023).

49. H. Yuk, J. Wu, X. Zhao, Hydrogel interfaces for merging humans and machines. *Nat. Rev. Mater.* **7**, 935–952 (2022).

50. Q. Huang, Z. Zheng, Pathway to developing permeable electronics. *ACS Nano* **16**, 15537–15544 (2022).

51. M. Bariya, L. Li, R. Ghattamaneni, C. H. Ahn, H. Y. Y. Nyein, L.-C. Tai, A. Javey, Glove-based sensors for multimodal monitoring of natural sweat. *Sci. Adv.* **6**, eabb8308 (2020).

52. J. Yi, G. Zou, J. Huang, X. Ren, Q. Tian, Q. Yu, P. Wang, Y. Yuan, W. Tang, C. Wang, L. Liang, Z. Cao, Y. Li, M. Yu, Y. Jiang, F. Zhang, X. Yang, W. Li, X. Wang, Y. Luo, X. J. Loh, G. Li, B. Hu, Z. Liu, H. Gao, X. Chen, Water-responsive supercontractile polymer films for bioelectronic interfaces. *Nature* **624**, 295–302 (2023).

53. C. Boehler, S. Carli, L. Fadiga, T. Stieglitz, M. Asplund, Tutorial: Guidelines for standardized performance tests for electrodes intended for neural interfaces and bioelectronics. *Nat. Protoc.* **15**, 3557–3578 (2020).

54. J. Deng, H. Yuk, J. Wu, C. E. Varela, X. Chen, E. T. Roche, C. F. Guo, X. Zhao, Electrical bioadhesive interface for bioelectronics. *Nat. Mater.* **20**, 229–236 (2021).

55. Q. Zhang, Y. Yang, D. Suo, S. Zhao, J. C.-W. Cheung, P. H.-M. Leung, X. Zhao, A biomimetic adhesive and robust Janus patch with anti-oxidative, anti-inflammatory, and anti-bacterial activities for tendon repair. *ACS Nano* **17**, 16798–16816 (2023).

56. V. K. Truong, A. Hayles, R. Bright, T. Q. Luu, M. D. Dickey, K. Kalantar-Zadeh, K. Vasilev, Gallium liquid metal: Nanotoolbox for antimicrobial applications. *ACS Nano* **17**, 14406–14423 (2023).

57. Q. Zhang, Y. Luo, B. Liang, D. Suo, S. Lyu, Y. Wang, X. Zhao, An anti-bacterial and anti-cancer fibrous membrane with multiple therapeutic effects for prevention of pancreatic cancer recurrence. *Biomater. Adv.* **137**, 212831 (2022).

58. T. Ahmad, Reviewing the tannic acid mediated synthesis of metal nanoparticles. *J. Nanotechnol.* **2014**, 954206 (2014).

59. A. Baldwin, B. W. Booth, Biomedical applications of tannic acid. *J. Biomater. Appl.* **36**, 1503–1523 (2022).

60. İ. Gülçin, Z. Huyut, M. Elmastaş, H. Y. Aboul-Enein, Radical scavenging and antioxidant activity of tannic acid. *Arab. J. Chem.* **3**, 43–53 (2010).

61. R. Defrin, A. Ohry, N. Blumen, G. Urca, Sensory determinants of thermal pain. *Brain* **125**, 501–510 (2002).

62. N. A. Martin, S. Falder, A review of the evidence for threshold of burn injury. *Burns* **43**, 1624–1639 (2017).

63. R. S. Johansson, A. B. Vallbo, Tactile sensibility in the human hand: Relative and absolute densities of four types of mechanoreceptive units in glabrous skin. *J. Physiol.* **286**, 283–300 (1979).

64. D. S. Louis, T. L. Greene, K. E. Jacobson, C. Rasmussen, P. Kolowich, S. A. Goldstein, Evaluation of normal values for stationary and moving two-point discrimination in the hand. *J. Hand Surg. Am.* **9**, 552–555 (1984).

65. S. Thube, M. R. Shah, P. H. Kothari, V. Shah, Assessment of two point discrimination on hand in adult population: An observational study. *Int. J. Health Sci. Res.* **10**, 60–63 (2020).

66. M. Ganji, A. Tanaka, V. Gilja, E. Halgren, S. A. Dayeh, Scaling effects on the electrochemical stimulation performance of Au, Pt, and PEDOT:PSS electrocorticography arrays. *Adv. Funct. Mater.* **27**, 1703019 (2017).

67. S. Cai, P. Ke, T. Narumi, K. Zhu, "ThermAirGlove: A pneumatic glove for thermal perception and material identification in virtual reality," in *2020 IEEE Conference on Virtual Reality and 3D User Interfaces (VR)* (IEEE, Atlanta, GA, USA, 2020), pp. 248–257. https://ieeexplore.ieee.org/document/9089505/.

68. Y. Tanaka, A. Shen, A. Kong, P. Lopes, "Full-hand electro-tactile feedback without obstructing palmar side of hand," in *Proceedings of the 2023 CHI Conference on Human Factors in Computing Systems* (Association for Computing Machinery, New York, NY, USA, 2023); *CHI '23*, pp. 1–15.

69. C. Cao, H. Liu, Y. Zhang, W. Jia, L. Zhang, H. Bao, A seamless, large-area silk-based interface for immersive on-palm tactile feedback. *Adv. Mater. Technol.* **9**, 2301599 (2024).

70. Y. Luo, C. Liu, Y. J. Lee, J. DelPreto, K. Wu, M. Foshey, D. Rus, T. Palacios, Y. Li, A. Torralba, W. Matusik, Adaptive tactile interaction transfer via digitally embroidered smart gloves. *Nat. Commun.* **15**, 868 (2024).

71. C. V. Keef, L. V. Kayser, S. Tronboll, C. W. Carpenter, N. B. Root, M. Finn III, T. F. O'Connor, S. N. Abuhamdieh, D. M. Davies, R. Runser, Y. S. Meng, V. S. Ramachandran, D. J. Lipomi, Virtual texture generated using elastomeric conductive block copolymer in a wireless multimodal haptic glove. *Adv. Intell. Syst.* **2**, 2000018 (2020).

72. W. Lin, D. Zhang, W. W. Lee, X. Li, Y. Hong, Q. Pan, R. Zhang, G. Peng, H. Z. Tan, Z. Zhang, L. Wei, Z. Yang, Super-resolution wearable electrotactile rendering system. *Sci. Adv.* **8**, eabp8738 (2022).